

Origin of enhanced electromechanical coupling in YbAlN alloy nitrides

Junjun Jia*

*Global Center for Science and Engineering (GCSE),
Faculty of Science and Engineering, Waseda University,
3-4-1 Okubo, Shinjuku, Tokyo 169-8555, Japan.*

Takahiko Yanagitani†

*Graduate School of Advanced Science and Engineering,
Waseda University, 3-4-1 Okubo, Shinjuku, Tokyo 169-8555, Japan
Kagami Memorial Research Institute for Materials Science and Technology,
Waseda University, 2-8-26 Nishiwaseda, Tokyo 169-0051, Japan and
JST PRESTO, 4-1-8 Honcho, Kawaguchi, Saitama 332-0012, Japan.*

(Dated: December 23, 2024)

Our experiments demonstrate that alloying the cubic-phase YbN into the wurtzite-phase AlN results in clear mechanical softening and enhanced electromechanical coupling of AlN. The first principle calculations reproduce experimental results well, and predict a maximum of 270% increase in electromechanical coupling coefficient caused by 1) enhanced piezoelectric response induced by the local strain of Yb ions and 2) structural flexibility of the YbAlN alloy. Extensive calculations suggest that the substitutional neighbor Yb–Yb pairs in wurtzite AlN are energetically stable along c axis, and avoid to form on the basal plane of wurtzite structure due to the repulsion between them, which explains that YbAlN films with high Yb concentrations are difficult to fabricate in our sputtering experiments. Moreover, the neighbor Yb–Yb pair interactions also promote structural flexibility of YbAlN, and are considered a cause for mechanical softening of YbAlN.

I. INTRODUCTION

AlN films have attracted considerable research interest for applications in electroacoustic devices, e.g., AlN film bulk acoustic resonator (FBAR) in microwave communication, because of their high thermal stability, and high operating frequencies, high Q factor, and high reliability.[1–3] A major drawback is its low electromechanical coupling coefficient k_t^2 , which is considerably smaller than those of perovskite-based oxides,[3, 4] which leads to loss in the microwave and low-bandwidth filters. The common experimental approach to improve k_t^2 is to alloy AlN with rocksalt nitrides (ScN, YN, and $\text{Ti}_{0.5}\text{Mg}_{0.5}\text{N}$).[5–8] A successful example is AlN alloying with rocksalt structured ScN, donated as ScAlN ($\text{Sc}_x\text{Al}_{1-x}\text{N}$), which shows a considerable enhancement in k_t^2 at $x=0.43$. [9]

From the perspective of materials design, when alloying with rocksalt nitrides, a giant enhancement in k_t^2 can be considered as 1) an increase in the field-induced strain *via* the increase in the longitudinal piezoelectric constant e_{33} , and 2) the simultaneous decrease in the longitudinal elastic stiffness c_{33} based on $k_t^2 \sim e_{33}^2/\epsilon_{33}c_{33}$, where ϵ_{33} is the dielectric constant.[10] In the ScAlN alloy, the enhancement in k_t^2 can be attributed to the giant piezoelectric response and mechanical softening due to the structural frustration, when the rocksalt endmember ScN is added to the alloy near phase boundary ($\sim 50\%$) between wurtzite and cubic phases.[12] In spite of the

giant piezoelectric response near phase boundary, the stability of the wurtzite phase at such high Sc concentrations is rather poor due to thermodynamic driving forces for phase separation, which leads to destruction of the piezoelectricity.[11] To improve the stability of the wurtzite phase during the fabrication, a feasible approach is to discover the alloy system with the low wurtzite-to-rocksalt transition concentration, which is expected to fabricate more easily.[12] Likewise, as an indication for mechanical softening, the elastic constant c_{33} for ScAlN decreases from 342 to 130 GPa with Sc dopant increasing from 0% to 50%.[7] The significant softening near phase boundary causes a reduction in the common figure of merit of the resonator,[13] and thus makes the material less attractive for practical applications.[14]

Alloying AlN with transition-metal nitrides as alternative materials to ScAlN have been explored to investigate. Theoretical calculations indicate that alloying AlN with CrN (CrAlN) or YN (YAlN) produces comparable e_{33} and c_{33} with ScAlN, and is expected to generate a high k_t^2 . However, to our best knowledge including our experiments, so far, no any experimental evidence shows that their k_t^2 values increase with the increase in the alloying element concentration as ScAlN does. In particular, an opposite behavior for CrAlN was observed that k_t^2 values decrease with increasing CrN concentration, which is possibly due to phase transition from a piezoelectric to a non-piezoelectric crystal phase.[15] Therefore, important aspects of electromechanical coupling in AlN-based piezoelectric materials require both experimental investigation and theoretical calculation.

In order to achieve the high k_t^2 value with low alloying concentration, a reasonable approach is to substitution-

* jia@aoni.waseda.jp

† yanagitani@waseda.jp

ally dope AlN by using the impurity element with larger ionic radius and different electronic configuration. Following the abovementioned scenario, alloying AlN with YbN, designated as YbAlN ($\text{Yb}_x\text{Al}_{1-x}\text{N}$), is expected to cause a similar structural frustration to produce the mechanical softening, since YbN also has a rocksalt cubic structure ($\text{Fm}\bar{3}\text{m}$, 225), where Yb^{3+} is bonded to six equivalent N^{3-} ions and form a mixture of corner- and edge-sharing YbN_6 octahedra. Nevertheless, Yb has a $[\text{Xe}]4f^{14}6s^2$ electronic configuration different from $[\text{Ne}]3s^23p^1$ of Al, and has a larger atomic radius than the reported transition metal nitride endmembers (ScN and CrN).[5–7] These characteristics are considered to generate the resistance to plastic deformation and thus mitigate the excessive softening. Moreover, a larger atomic radius would be expected to produce a large internal strain, which possibly induces an increase in e_{33} .

In this study, we investigated electromechanical coupling phenomenon in YbAlN from both experimental and theoretical aspects, and demonstrated that alloying the cubic YbN into the wurtzite AlN leads to clear mechanical softening and enhanced e_{33} , which improves k_t^2 up to $\sim 10\%$, which is close to the reported value of 15.5% for ScAlN.[9] We also provided a fundamental understanding of such dramatic enhancement in electromechanical coupling for YbAlN.

II. EXPERIMENTAL AND COMPUTATIONAL DETAILS

The combinatorial synthesis of c -axis oriented YbAlN films were fabricated by sputtering deposition. YbAlN films were deposited on Ti electrode film/silica glass substrate, where a highly oriented (0001) Ti electrode film was used as the under-layer electrode to form the HBAR structure. The film structure was characterized by X-ray diffraction (XRD) with a 2θ - ω configuration (X'Pert PRO, PANalytical). The Yb concentrations were analyzed by electron probe microanalysis (EPMA) (JXA-8230, JEOL). The k_t^2 values and the film density were determined by comparing the experimental and theoretical longitudinal wave conversion loss curve *vs* the frequency of HBAR resonators.[3, 16]

For theoretical calculations, the structures representing hexagonal YbAlN alloys up to $x=0.45$ were first relaxed using density functional theory. The Vienna Ab-initio Simulation Package (VASP)[17] was used for structural optimization, using the generalised gradient approximation (GGA) as parameterized by Perdew *et al.* for the exchange-correlation potential.[18] A $3 \times 3 \times 2$ supercell was selected, and the special quasirandom structure (SQS)[19–21] method was used to model the random distribution of Yb in the wurtzite YbAlN structure with different x values. The SQSs were generated by optimizing the locations of Yb atoms to minimize the Warren–Cowley pair short range order parameters, which were calculated up to the 6th coordination shell. Moreover, to

realistically simulate the chemical disorder of actual alloy nitrides, we constructed ~ 10 SQS structures with the same Yb concentration, and selected the SQS structure with the minimum total formation energy to calculate piezoelectric and elastic tensors. The Monkhorst-Pack k -point grids were set to $3 \times 3 \times 3$. The plane wave basis set with a cutoff energy of 600 eV was adopted, and the total energies were converged to less than 10^{-9} eV for structural relaxation. The elastic and piezoelectric tensors were calculated using density-functional perturbation theory.[22–25]

III. RESULTS AND DISCUSSION

A. Structural Characteristics

All fabricated YbAlN films were oriented along c -axis with various rocking curve full width at half maximum (FWHM), as shown in Fig. 3. No any phases from Yb or YbN can be found in the XRD pattern.

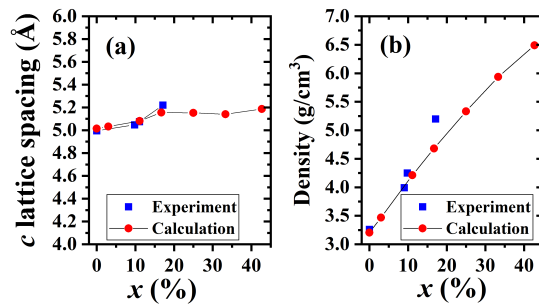


FIG. 1. The c lattice spacing (a) and density (b) of YbAlN films from experimental measurement and theoretical calculation. The solid square represents the measurement values, and the solid circle shows the calculated values. Note that YbAlN films with high Yb concentrations ($x > 0.25$) are difficult to fabricate by sputtering.

The calculated lattice parameters of wurtzite AlN are $a=3.128$ Å and $c=5.015$ Å, which are close to reported experimental and theoretical values.[26, 27] Table I shows the calculated lattice constants of YbAlN. Both a - and c -axis lattice spacings monotonically increase with an increase in the Yb concentration due to the substitution of Yb^{3+} ion (ionic radius: 0.87 Å) into the host Al ion (ionic radius: 0.54 Å). Whereas, XRD patterns show a similar tendency, where the (0002) plane gradually shifts toward the low-angle side, demonstrating that Yb atoms are substituted into host Al sites during the nucleation and/or growth. The extrapolated c -lattice constants from the precise XRD measurements are consistent with ones from our first principle calculations, as shown in Fig. 1. Moreover, our calculations show a decreasing trend in the c/a ratio, which suggests that an increase in lattice spacing in a axis is larger than the one in c axis.

TABLE I. Calculated structural parameters of YbAlN.

	a (Å)	c (Å)	c/a	ρ (g/cm ³)
AlN	3.128	5.015	1.603	3.203
$x=0.03$	3.146 \pm 0.000	5.032 \pm 0.000	1.600	3.469
$x=0.11$	3.201 \pm 0.001	5.081 \pm 0.002	1.596	4.211
$x=0.17$	3.234 \pm 0.005	5.156 \pm 0.004	1.602	4.679
$x=0.25$	3.295 \pm 0.007	5.153 \pm 0.016	1.568	5.332
$x=0.33$	3.357 \pm 0.024	5.141 \pm 0.010	1.523	5.935
$x=0.43$	3.408 \pm 0.006	5.187 \pm 0.014	1.523	6.490

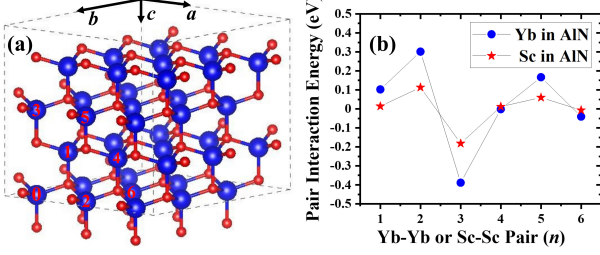


FIG. 2. (a) the six pair configurations in the $3 \times 3 \times 2$ supercell (Purple: Al, and Brown: N atoms). A Yb-Yb pair (n) is defined as the two n th neighbor substitutional Yb atoms relative to a Yb atom located at the origin “O”. (b) The pair interaction energies $\Delta E^{(n)}$ for $n=1, 2, 3, 4, 5, 6$ th neighbor Yb pairs. For comparison, $\Delta E^{(n)}$ in Sc doped AlN was also calculated.

We next inquire why the c/a ratio decreases as x increases. Let’s start from the questions what is the energetics involved in finding two substitutional Yb atoms in the wurtzite AlN structure. From this aspect, we calculated the pair interaction energy $\Delta E^{(n)}$ as the difference between the total energy of two n th neighbor Yb atoms and for two Yb atoms at infinite separation (twice the energy of an isolated Yb atom),[28] i.e.,

$$\Delta E^{(n)} = \left[E(\text{Al}_{\frac{m}{2}}\text{N}_{(\frac{m}{2}-2)}\text{Yb}_2) + E(\text{Al}_{\frac{m}{2}}\text{N}_{\frac{m}{2}}) \right] - 2E(\text{Al}_{\frac{m}{2}}\text{N}_{(\frac{m}{2}-1)}\text{Yb}), \quad (1)$$

where n denotes the pair index, and $m=72$ is the number of atoms in the supercell. The energies correspond to the fully relaxed supercell calculations. In the calculations, an identical k -mesh ($3 \times 3 \times 3$) is applied for all three total energies for consistency. The lattice parameter for all supercells has been chosen to correspond to the theoretical AlN lattice constants.

The $\Delta E^{(n)}$ is shown in Fig. 1. The result for $\Delta E^{(n=3)}$ is negative (-0.38 eV), indicating that the binding between the Yb atoms along c axis is energetically stable. $\Delta E^{(n=4)}$ and $\Delta E^{(n=6)}$ are close to zero, but remains negative. Whereas, the positive $\Delta E^{(n)}$ for $n=1, 2$, and 5 indicates the repulsive interaction between the Yb atoms at these positions. Here, the attractive pair interaction is considered to induce the compressive stress along the c axis ($n=3$), and the repulsive pair interaction ($n=2$) is

expected to give rise to the tensile stress along the basal plane. Thus, their superposition leads to a decreasing c/a ratio with increasing x . Note that the calculation results for $\Delta E^{(n)}$ using a bigger supercell ($5 \times 5 \times 3$) with $a=15.64$ Å and $c=15.04$ Å show the same tendency, suggesting that $\Delta E^{(n)}$ is an intrinsic physical parameter for the YbAlN alloy.

Moreover, the pair interaction energies would suggest that Yb-Yb pairing avoids $n=1, 2$, and 5 th neighbor shells, and favors $n=3, 4$ and 6 th neighbor configurations, especially $n=3$. $\Delta E^{(n)}$ in ScAlN shows the similar trends but has smaller value. For a growth process under thermal equilibrium, the Yb atoms should most likely pair into the third nearest neighbor configurations (namely Yb-Yb pairing along c axis) rather than be randomly distributed. This also explains our experimental observations that YbAlN films with high Yb concentrations ($x > 0.25$) are difficult to fabricate in sputtering experiments because the repulsion among Yb dopants in the basal plane suppresses Yb substitution into Al sites. A similar repulsion among dopants is also present in Sn-doped In_2O_3 . [29–31]

Based on the above results, a SQS cell with the random distribution of Yb atoms cannot model the spatial configuration of Yb atoms in wurtzite AlN. In this study, we constructed ~ 10 different SQS structures with the same Yb concentration, and selected the SQS structure with the minimum total formation energy to calculate its piezoelectric and elastic tensors.

B. Electromechanical Coupling

Since the accurate measurement of c_{33} and e_{33} along c direction for nitride alloy films is quite difficult, especially for the thin films with the thickness of several hundred nanometers, in this study, the experimentally measured k_t^2 and acoustic wave velocity V were directly compared with the theoretically calculated values.

Because k_t^2 is known to be approximately equal to the longitudinal electromechanical coupling coefficient k_{33}^2 for the c -oriented AlN films,[10] k_t^2 can be estimated by $k_t^2 \sim k_{33}^2 = e_{33}^2/\epsilon_{33}c_{33}$. In Fig. 3 (a), the measured k_{33}^2 values are compared with the calculated values. The calculated k_{33}^2 are in good agreement with the experimentally measured k_t^2 up to approximately $x \sim 0.12$, where the YbAlN films fabricated at various conditions show a saturation k_{33}^2 value of 9.05% at approximately $x \sim 0.12$. In contrast, our theoretical calculations suggest the maximal k_{33}^2 of 17.6% at $x=0.33$. At high Yb concentration ($x > 0.12$), k_{33}^2 is larger than those calculated ones. The experimentally determined k_{33}^2 often depends on the crystallinity of thin films and the crystal orientation, as well as the polarization direction. Moreover, as revealed by the calculations of the pair interaction energies, the repulsion between Yb-Yb pairs on the basal plane is considered to hinder further substitutional Yb doping.

Acoustic wave velocity is also a measurable experimen-

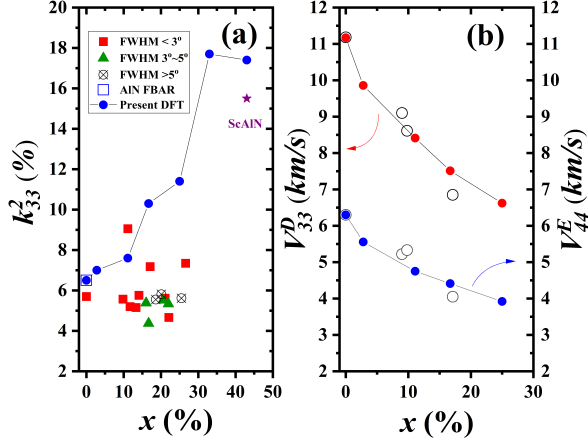


FIG. 3. (a) The calculated k_{33} values are compared with the experimentally determined ones for YbAlN films with different rocking curve FWHMs. The smaller is the FWHM, the stronger is the c -axis orientation. (b) The calculated V_{33} and V_{44} values are compared with the experimentally measured V_{33}^E and V_{44}^E for YbAlN films with $\text{FWHM} < 3^\circ$, respectively. Connected lines represent the calculated values, whereas the scattered points show the experimentally measured ones. In Fig. (a), the symbol \square represents the measurement value for the general pure AlN FBAR with Mo electrodes, and the symbol \star shows the k_t^2 value for ScAlN at $x=43\%$. [9]

tal quantity, and it can be precisely determined by acoustic wave resonance spectra.[32] Under a constant external electric field, elastic constants (c_{33}^E and c_{44}^E) can be experimentally determined by the following equations,

$$c_{33}^E = \rho(V_{33}^D)^2(1 - k_{33}^2) \quad (2)$$

and

$$c_{44}^E = \rho(V_{44}^E)^2, \quad (3)$$

where ρ is the density, and V_{33}^D and V_{44}^E are longitudinal and shear acoustic wave velocities, respectively. In Fig. 3 (b), the calculated V_{33} and V_{44} values are consistent with experimentally measured V_{33}^E and V_{44}^E values, respectively. Such quantitative agreement between our calculation (0 K) and experimental results measured at room temperature allows us to expect that acoustic phonon contribution to piezoelectricity in YbAlN alloys is small up to room temperature.

Based on the quantitative agreement between our calculation and experimentally measured results, we investigated the microscopic mechanism for the k_t^2 change with Yb concentration. The calculated dielectric constants, piezoelectric constants, and elastic moduli for YbAlN with different x are listed in Table II. With an increase in the Yb concentration, c_{33} linearly decreases up to $x=33\%$, and a slowdown is observed from $x=33\%$ to 43% .

Our calculations reproduce the changing behavior of c_{33}^E and c_{44}^E well. Moreover, an increase in e_{33} with the alloying Yb concentration is accompanied by a decrease in c_{33} ; thus, the increasing piezoelectric response and mechanical softening are considered to cooperate to cause an increase in k_t^2 in YbAlN films.

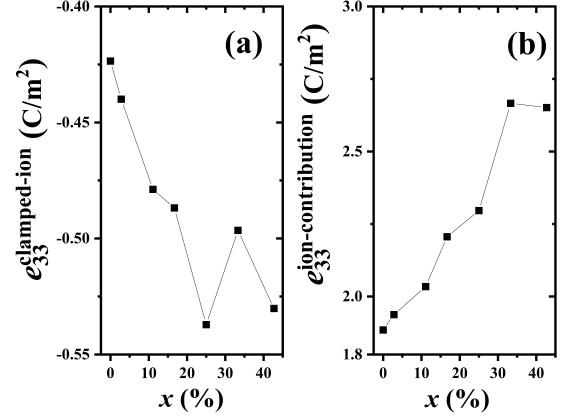


FIG. 4. Calculated contributions of e_{33} introduced in Eq. (3). (a) the *clamped-ion* contribution, and (b) the ionic contribution, which is related to the strain effect and the Born charges Z_{33} calculated from Eq. (3).

Moreover, from the microscopic perspective, e_{33} can be divided into two main contributions: 1) electronic response to the strain of the crystal structure (*clamped-ion* term), and 2) the effect of internal strain on piezoelectric polarizations.[27, 33] Therefore, e_{33} can be expressed as follows:

$$e_{33}(x) = e_{33}^{\text{clamped-ion}}(x) + \frac{4eZ_{33}(x)}{\sqrt{3}a(x)^2} \frac{du}{d\sigma}, \quad (4)$$

where e is the elementary charge, a represents the equilibrium lattice parameter, Z represents the dynamical Born or transverse charge in units of e , and σ is the macroscopic applied strain. The wurtzite internal parameter is described by u , where the layered hexagonal phase differs from the wurtzite structure only in the internal parameter u between metal and nitrogen sublattices ($u=0.5$ for the hexagonal phase, and $u \neq 0.5$ for the wurtzite phase). In Fig. 4 (a), a monotonic decrease was observed for the *clamped-ion* term up to $x=0.25$, followed by an increase up to -0.49 C/m² at $x=0.33$. In comparison, the ionic contribution for e_{33} , which represents the local structural sensitivity to macroscopic axial strain σ , shows clear increase with an increase in the Yb concentration in Fig. 4 (b). Thus, an increased piezoelectric response should be mainly attributed to the internal structural strain.

To understand the ionic contribution to the piezoelectricity of YbAlN, we calculated the compositional

TABLE II. Elastic (c_{ij}) and piezoelectric (e_{ij}) constants of YbAlN with different Yb concentration x , where c_{33}^E and c_{44}^E are the experimental values by measuring YbAlN films with FWHM $<3^\circ$ in this study. Elastic constants are in GPa, and piezoelectric constants are in C/m². The calculated and measured c_{ij} and e_{ij} values for AlN from other groups are provided for comparison, and our calculations agree well with previous ones.[27, 36] Note that ϵ_{33} is the 33 component of the dielectric tensor.

AlN	ϵ_{33}	c_{11}	c_{12}	c_{13}	c_{33}	c_{44}	c_{33}^E	c_{44}^E	e_{31}	e_{33}	k_{33}^2 (%)
This study											
AlN	9.76	375	128	98	355	112	380	127	-0.58	1.46	6.5
$x=0.03$	9.97	360	128	102	337	107	—	—	-0.58	1.50	7.0
$x=0.11$	11.16	312	124	105	298	95	302	109	-0.63	1.56	7.6
$x=0.17$	10.99	294	129	113	264	91	207	78	-0.59	1.72	10.3
$x=0.25$	11.67	276	123	116	234	82	—	—	-0.59	1.76	11.4
$x=0.33$	12.84	255	139	119	192	85	—	—	-0.68	2.17	17.7
$x=0.43$	13.15	231	126	117	182	77	—	—	-0.65	2.12	17.4
References for AlN											
Measured by Tsubouchi et al. ^a	—	345	125	120	395	118	—	—	—	—	—
Measured by McNeil et al. ^b	—	411 \pm 10	149 \pm 10	99 \pm 4	389 \pm 10	125 \pm 5	—	—	—	—	—
Calculated by Xie et al. ^c	—	376	126	98	356	116	—	—	—	—	—
Calculated by Bernardini et al. ^d	—	—	—	—	—	—	—	—	-0.60	1.46	—

^a Reference. [34].

^b Reference. [35].

^c Reference. [36].

^d Reference. [27].

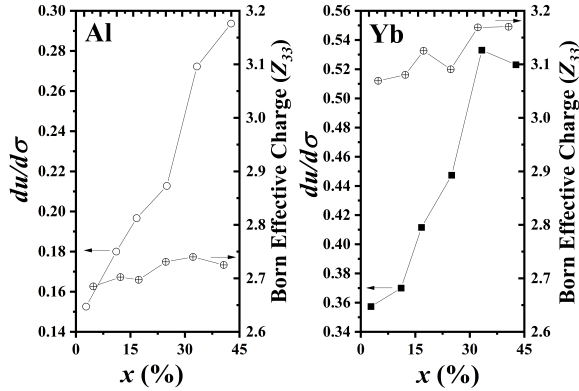


FIG. 5. Compositional weighted and site resolved internal strain sensitivity and Born effective charges of YbAlN.

weighted and site resolved internal strain sensitivity and dynamic Born charge. Fig. 5 displays that the internal strain sensitivity ($du/d\sigma$) around both Al and Yb sites increases as the Yb concentration increases, and the structural strain sensitivity around Yb sites is approximately two times larger than that around Al sites under different Yb concentrations. On the other hand, Z_{33} for Yb ions remains at ~ 3.1 , and Z_{33} for Al ions keeps at ~ 2.7 , which vary within approximately 10% around the ionic nominal value of 3. Larger Z_{33} indicates that the Yb ion has a large polarization response to the external electric field. The abovementioned comparison suggests that the change in the ionic contribution is mainly dominated by

local structural distortion caused by alloying Yb.

C. Mechanical Softening

From the structural point of view, AlN has a wurtzite structure (6mm, 226), where Al³⁺ is bonded to four equivalent N³⁻ to form a corner-sharing tetrahedral structure, and YbN has a cubic structure (Fm $\bar{3}$ m, 225) with a mixture of corner- and edge-sharing octahedral structure YbN₆. The substitution of the Yb atom in Al sites is presumed to lead to structural flexibility, and then causes mechanical softening. Herein, we investigated the potential energy landscape of YbAlN at $x=0.33$, which, in theory, has the maximal k_t^2 value.

In Fig. 6, the potential energy landscape exhibits a flat, elongated structure, which is derived by the interpolation of energy points in the (*volume*, *c/a* ratio) space. This landscape pattern differs from that of well-studied ScAlN.[33] In the ScAlN alloy system, the Sc atoms prefer to bind hexahedrally to nitrogen, and the resultant hexagonal ScN phase is energetically close to the wurtzite AlN phase, which acts as an energy saddle point.[33, 37]

To reveal the mechanical softening mechanism in the YbAlN alloy system, we investigated the local structure of the Yb atom. In the relaxed YbAlN structure ($x=0.33$ and $c/a=1.52$), clear local structural distortion around Yb ion is observed, which differs from the local structure of the Al ion, as shown in Fig. 7. Depending on different local chemical environments, the Yb-N(1) bond length varies from 2.152 to 2.336 Å with an average of 2.214 Å, and the Yb-N(3) bond length varies from 2.073 to 2.279 Å with an average of 2.172 Å. Notably, Al-N tetrahe-

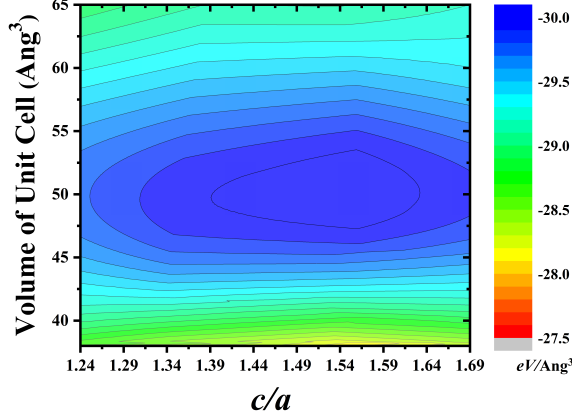


FIG. 6. Energy landscape of wurtzite YbAlN ($x=0.33$).

dral bond lengths are 1.913 Å in the parent wurtzite AlN structure, and the longer Yb–N(1) and Yb–N(3) bond lengths in the tetrahedral Yb³⁺ structure are due to a larger ionic radius and more widely extended electronic orbitals of Yb ions (principal quantum number $n=6$). Moreover, the Yb–N(2) bond length varies from 2.540 to 3.249 Å with an average of 2.963 Å. The obvious difference between Yb–N(1) and Yb–N(2) ($u \neq 0.5$) suggests YbAlN ($x=0.33$) maintains piezoelectric crystal phase. Furthermore, when the c/a ratio is compressed to 1.40, which is around the edge of the lowest energy contour in Fig. 6, the shortest bond lengths of Yb–N(3) on the basal plane is 2.023 Å, and the shortest bond lengths of Yb–N(1) is 2.142 Å. The shortest bond length of Yb–N(2) is 2.356 Å, comparable with the theoretical Yb–N bond length (2.464 Å) in the cubic YbN structure. Instead of YbN₄ tetrahedral structure, the local structure of Yb³⁺ seems to have a deformed bipyramidal structure, which needs further investigation.

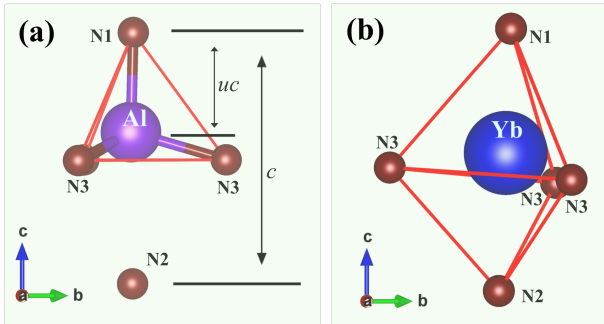


FIG. 7. Local structures of Yb and Al atoms in the relaxed YbAlN alloy system ($x=0.33$, and $c/a=1.52$). The index of nitrogen atoms in the local structure is given. The deformed bipyramidal structure in Fig. (b) is shown just for the eye-guide.

Based on the difference in the bond length between Yb–N(1) and Yb–N(2) under external pressure ($c/a=1.40$), a decrease in the c/a ratio with increasing x in Table I cannot be connected to the phase transition from the wurtzite ($u=0.5$) to a quasi-stable layered hexagonal phase ($u \neq 0.5$), as those in ScAlN.[33] Alternatively, the mechanical softening of YbAlN is attributed to structural flexibility, which is considered from the change of chemical bond type and/or orientation as well as the local structure after alloying with YbN, which flattens the energy potential landscape. Structural flexibility is beneficial to the change of wurtzite YbAlN toward a layered hexagonal phase under external pressure.

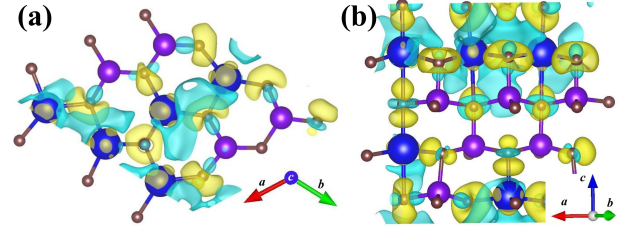


FIG. 8. Charge density differences of YbAlN with $x=0.33$ under the compressed state of $c/a=1.40$. (a) a ab basal plane is selected, and (b) a ac plane is selected to show charge density difference along c axis. The loss of electrons is indicated in light-blue color, and electron accumulation is indicated in yellow. Each isovalue is set to 10% of the maximum. (Purple: Al, Blue: Yb, and Brown: N atoms)

To gain more microscopic insights about the mechanical softening, the charge density difference is calculated to study the chemical interaction among constituent atoms in YbAlN with $x=0.33$. We define the charge density difference as $\delta\rho = \rho_t - \rho_1 - \rho_2$, where ρ_t , ρ_1 , and ρ_2 are the charge densities of YbAlN, AlN, and isolated Yb atoms, respectively. In Fig. 8 (a), the results of the redistribution of charge density obtained by ab initio calculation show that there is considerable loss of electrons between two adjacent Yb³⁺ ions, implying the existence of the repulsion between adjacent Yb³⁺ ions, which is also revealed in the calculations of the pair interaction energy ($\Delta E^{(n=2)}$) as shown in Fig. 1 (b). For wurtzite structure, any two identical substitutional Yb ions on the ab basal plane experience elastic repulsion due to the fact that the Al ions between them have to relax away from the closest Yb ions (Yb³⁺ has a larger ionic size), and hence the total energy increases, i.e. repulsion. In contrast, Fig. 8 (b) displays that a deformed bipyramidal structure can be formed in the certain local chemical environment, i.e. a chain configuration (–Yb–N–Yb–) along c axis, where charges are accumulated on both sides of N ions in the c direction with the bond lengths of 2.200 and 2.464 Å for Yb–N(1) and Yb–N(2), respectively. Such a chain configuration allows N ion to attract two nearby Yb ions, and causes a decrease in the total energy as revealed from the calculations of pair interaction energy

($\Delta E^{(n=3)}$). Owing to different bond lengths for Yb–N(1) and Yb–N(2), the deformed bipyramidal structure maintains the piezoelectricity along c axis.

In Table II, C_{11} and C_{33} rapidly decreases with increasing x , indicating structural flexibility along a -axis and c -axis direction for YbAlN under the external uniaxial stress, respectively. To understand the origin of structural flexibility at $x=0.33$, we calculated the pair interaction energy $\Delta E^{(n)}$ under different c/a ratios. Fig. 9 (a) displays that $\Delta E^{(3)}$ keeps negative down to $c/a=1.35$, and then changes to positive, indicating the elastic nature of the pair interactions (attraction and repulsion). When a Yb atom is substituted into Al site, a Yb–N(1) chemical bond is formed along c axis, and gives rise to the decrease in the total energy of the system, which has been demonstrated by our calculations (not shown here). A chain configuration of –Yb–N–Yb– can further reduce the total energy. Because the lattice spacing in a axis was fixed in the calculations, $\Delta E^{(2)}$ and $\Delta E^{(6)}$ almost remain the same positive values at all c/a ratios.

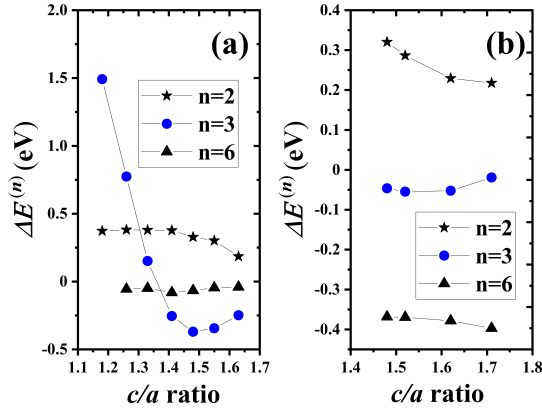


FIG. 9. Calculated pair interaction energies $\Delta E^{(n)}$ at different c/a ratios: (a) the lattice spacing in a axis is fixed, and (b) the lattice spacing in c axis is fixed. $\Delta E^{(3)}$ is the pair interaction energy due to the neighbor pair along c axis, and $\Delta E^{(2)}$ and $\Delta E^{(6)}$ are the pair interaction energies due to the neighbor pairs on the ab basal plane in wurtzite YbAlN. Here, a $3 \times 3 \times 2$ AlN structure with the lattice parameters of YbAlN ($x=0.33$) was selected as the reference, and a $3 \times 3 \times 3$ k -mesh was used for all the calculations.

On the other hand, Fig. 9 (b) displays that a strong repulsive interaction exists between Yb–Yb pair along a axis because $\Delta E^{(2)}$ keeps a large positive value for all c/a ratios with a fixed c lattice spacing. For wurtzite structure ($u \neq 0.5$), two nearby substitutional Yb ions on the basal plane experience elastic repulsion because 1) Yb³⁺ has a larger ionic size than Al³⁺ and 2) N ions are not on the same basal plane with Yb ions. In fact, any two identical substitutional Yb ions on the basal plane should experience elastic repulsion due to the fact that the Al ions between Yb ions have to relax away from the closest Yb ions, and hence the total energy increases, i.e. repulsion. Because the elastic nature of the attraction or the repulsion as shown in Fig. 9, the Yb–Yb pair interactions are considered a cause of structural flexibility in YbAlN.

IV. CONCLUSION

Our experiments show that alloying cubic YbN into wurtzite AlN leads to enhanced electromechanical coupling in AlN, where k_t^2 is improved by 150% at $x \sim 11\%$. Theoretical calculations agree well with experimentally measured k_t^2 and elastic constants, suggesting that electromechanical coupling is mainly dominated by the local strain around Yb ions and structural flexibility caused by Yb substitution into host Al sites. Introducing more YbN into the AlN system induces mechanical softening up to $x=42\%$. Our calculations indicate that the Yb–Yb pair interactions can contribute to such mechanical softening. The calculations of pair interaction energies also show that the Yb–Yb pairing avoids $n=1, 2$, and 5th nearest neighbor configurations, and favors $n=3, 4$, and 6th neighbor configurations, especially $n=3$, i.e. the Yb–Yb pair along c axis. Alloying AlN with YbN is promising, and offers an increased k_t^2 up to $\sim 10\%$, even at a rather low Yb concentration ($\sim 11\%$), which is comparable with that of commercial ScAlN films.

V. ACKNOWLEDGMENTS

T. Yanagitani thanks the support from JST CREST (Grant No. JPMJCR20Q1), Japan. J. Jia acknowledges the funding from JSPS KAKENHI Grant-in-Aid for Scientific Research (C) (Grant No. 20K05368).

-
- [1] A. Muller, D. Neculoiu, G. Konstantinidis, A. Stavrinidis, D. Vasilache, A. Cismaru, M. Danila, M. Dragoman, G. Deligeorgis, and K. Tsagaraki, 6.3-GHz film bulk acoustic resonator structures based on a gallium nitride/silicon thin membrane, *IEEE Electron Device Lett.* **30**, 799 (2009).
 - [2] T. Yokoyama, Y. Iwazaki, T. Nishihara, M. Ueda, Analysis on electromechanical coupling coefficients in

AlN-based bulk acoustic wave resonators based on first-principle calculations, 2012 IEEE International Ultrasonics Symposium, IEEE (2012), 10.1109/ULT-SYM.2012.0137.

- [3] T. Yanagitani and M. Suzuki, Enhanced piezoelectricity in YbGaIn films near phase boundary, *Appl. Phys. Lett.* **104**, 082911 (2014).

- [4] V. M. Ristic, Principles of acoustic devices, New York: Wiley, (1983).
- [5] M. Akiyama, T. Kamohara, K. Kano, A. Teshigahara, Y. Takeuchi, and N. Kawahara, Enhancement of piezoelectric response in scandium aluminum nitride alloy thin films prepared by dual reactive cosputtering, *Adv. Mater.* **21**, 593 (2009).
- [6] M. Akiyama, K. Kano, and A. Teshigahara, Influence of growth temperature and scandium concentration on piezoelectric response of scandium aluminum nitride alloy thin films, *Appl. Phys. Lett.* **95**, 162107 (2009).
- [7] C. Tholander, I. A. Abrikosov, L. Hultman, and F. Tasnádi, Volume matching condition to establish the enhanced piezoelectricity in ternary (Sc,Y)_{0.5}(Al,Ga,In)_{0.5}N alloys, *Phys. Rev. B* **87**, 094107 (2013).
- [8] C. Tholander, F. Tasnádi, I. A. Abrikosov, L. Hultman, J. Birch, and B. Alling, Large piezoelectric response of quaternary wurtzite nitride alloys and its physical origin from first principles, *Phys. Rev. B* **92**, 174119 (2015).
- [9] K. Umeda, H. Kawai, A. Honda, M. Akiyama, T. Kato, and T. Fukura, Piezoelectric properties of ScAlN thin films for piezo-MEMS devices, the 26th International Conference on Micro Electro Mechanical Systems (MEMS) (IEEE, Taipei, 2013), pp. 582–589.
- [10] M. Feneberg, and K. Thonke, Polarization fields of III–nitrides grown in different crystal orientations, *J. Phys. D: Appl. Phys.* **19**, 403201 (2007).
- [11] C. Höglund, J. Birch, B. Alling, J. Bareño, Z. Czigány, P. O. Persson, G. Wingqvist, A. Žukauskaitė, and L. Hultman, Wurtzite structure Sc_{1-x}Al_xN solid solution films grown by reactive magnetron sputter epitaxy: Structural characterization and first–principles calculations, *J. Appl. Phys.* **107**, 123515 (2010).
- [12] S. Manna, K. R. Talley, P. Gorai, J. Mangum, A. Zakutayev, G. L. Brennecke, V. Stevanović, and C. V. Ciobanu, Enhanced piezoelectric response of AlN via CrN alloying, *Phys. Rev. Applied* **9**, 034026 (2018).
- [13] R. R. Syms, H. Zou, and P. Boyle, Mechanical stability of a latching MEMS variable optical attenuator, *J. Microelectromech. Syst.* **14**, 529 (2005).
- [14] S. Manna, G. L. Brennecke, V. Stevanović, and C. V. Ciobanu, Tuning the piezoelectric and mechanical properties of the AlN system via alloying with YN and BN, *J. Appl. Phys.* **122**, 105101 (2017).
- [15] M. Suzuki and S. Kakio, Electromechanical coupling coefficient k_t^2 of Cr doped AlN films grown by sputtering deposition, 2019 IEEE International Ultrasonics Symposium (IUS), 2019, pp. 716–719, doi: 10.1109/ULTSYM.2019.8926302.
- [16] N. Iwata, S. Kinoshita, J. Jia, M. Suzuki, and T. Yanagitani, Experimental and theoretical investigation of k_t^2 and mechanical quality factor Q_m in YbAlN films using DFT, 2020 IEEE International Ultrasonic Symposium (IUS), 2020, pp. 1–2.
- [17] G. Kresse and J. Furthmüller, Efficiency of *ab-initio* total energy calculations for metals and semiconductors using a plane-wave basis set, *Comput. Mater. Sci.* **6**, 15 (1996).
- [18] J. P. Perdew, K. Burke, and M. Ernzerhof, Generalized gradient approximation made simple, *Phys. Rev. Lett.* **77**, 3865 (1996).
- [19] A. Zunger, S.-H. Wei, L. G. Ferreira, and J. E. Bernard, Special quasirandom structures, *Phys. Rev. Lett.* **65**, 353 (1990).
- [20] L. Chen, D. Holec, Y. Du, and P. H. Mayrhofer, Influence of Zr on structure, mechanical and thermal properties of Ti–Al–N, *Thin Solid Films* **519**, 5503 (2011).
- [21] A. van de Walle, P. Tiwary, M. de Jong, D. L. Olmsted, M. Asta, A. Dick, D. Shin, Y. Wang, L. -Q. Chen, Z. -K. Liu, Efficient stochastic generation of special quasirandom structures CALPHAD: Computer Coupling of Phase Diagrams and Thermochemistry **42**, 13 (2013).
- [22] D. Vanderbilt, Berry–phase theory of proper piezoelectric response, *J. Phys. Chem. Solids* **61**, 147 (2000).
- [23] X. Gonze, and C. Lee, Dynamical matrices, Born effective charges, dielectric permittivity tensors, and interatomic force constants from density–functional perturbation theory, *Phys. Rev. B* **55**, 10355 (1997).
- [24] X. Wu, D. Vanderbilt, and D. R. Hamann, Systematic treatment of displacements, strains, and electric fields in density–functional perturbation theory, *Phys. Rev. B* **72**, 035105 (2005).
- [25] R. D. King-Smith, and D. Vanderbilt, Theory of polarization of crystalline solids, *Phys. Rev. B* **47**, 1651 (1993).
- [26] N. S. van Damme, S. M. Richard, and S. R. Winzer, Liquid–phase sintering of aluminum nitride by Europium oxide additives, *J. Am. Ceram. Soc.* **72**, 1409 (1989).
- [27] F. Bernardini, V. Fiorentini, and D. Vanderbilt, Spontaneous polarization and piezoelectric constants of III–V nitrides, *Phys. Rev. B* **56**, R10024 (1997).
- [28] T. Mattila, A. Zunger, P–P and As–As isovalent impurity pairs in GaN: Interaction of deep t_2 levels, *Phys. Rev. B* **59**, 9943 (1999).
- [29] N. Yamada, I. Yasui, Y. Shigesato, H. Li, Y. Ujihira, and K. Nomura, Doping mechanism of Sn in In₂O₃ powder studied using ¹¹⁹Sn Mössbauer spectroscopy and X-ray diffraction, *Jpn. J. Appl. Phys.* **38**, 2856 (1999).
- [30] J. Jia, A. Takaya, T. Yonezawa, K. Yamasaki, H. Nakazawa, Y. Shigesato, Carrier densities of Sn–doped In₂O₃ nanoparticles and their effect on X–ray photoelectron emission, *J. Appl. Phys.* **125**, 245303 (2019).
- [31] J. Jia, S. Iwasaki, S. Yamamoto, S. Nakamura, E. Magome, T. Okajima, Y. Shigesato, Temporal evolution of microscopic structure and functionality during crystallization of amorphous indium-based oxide films, *ACS Appl. Mater. Interfaces* **13**, 31825 (2021).
- [32] Y. Ohashi, M. Arakawa, J. Kushibiki, B. M. Epelbaum, and A. Winnacker, Ultrasonic microspectroscopy characterization of AlN single crystals, *Appl. Phys. Express* **1**, 077004 (2008).
- [33] F. Tasnádi, B. Alling, C. Höglund, G. Wingqvist, J. Birch, L. Hultman, and I. A. Abrikosov, Origin of the anomalous piezoelectric response in wurtzite Sc_xAl_{1-x}N alloys, *Phys. Rev. Lett.* **104**, 137601 (2010).
- [34] K. Tsubouchi, K. Sugai, and N. Mikoshiba, AlN material constants evaluation and SAW properties on AlN/Al₂O₃ and AlN/Si, IEEE Ultrasonic Symposium, pp. 375, (1981).
- [35] L. E. McNeil, M. Grimsditch, R. H. French, Vibrational spectroscopy of aluminum nitride, *J. Am. Ceram. Soc.* **76**, 1132 (1993).
- [36] M. -Y. Xie, F. Tasnádi, I. A. Abrikosov, L. Hultman, and V. Darakchieva, Elastic constants, composition, and piezoelectric polarization in In_xAl_{1-x}N: From *ab initio* calculations to experimental implications for the applicability of Vegard’s rule *Phys. Rev. B* **86**, 155310 (2012).
- [37] N. Farrer, and L. Bellaiche, Properties of hexagonal ScN versus wurtzite GaN and InN, *Phys. Rev. B* **66**,

201203(R) (2002).